*J. Fluid Mech.* (2003), *vol.* 493, *pp.* 31–58.  
DOI: 10.1017/S0022112003005780 Printed in the United Kingdom

# On the linear stability of swept attachment-line boundary layer flow. Part 2. Non-modal effects and receptivity

By DOMINIK OBRIST† AND PETER J. SCHMID

Department of Applied Mathematics, University of Washington, Seattle, WA 98195-2420, USA
pjs@amath.washington.edu

(Received 17 January 2002 and in revised form 18 April 2003)

Following the study of the spectral properties of linearized swept Hiemenz flow (see Part 1, Obrist & Schmid 2003) we investigate the potential of swept Hiemenz flow to support transiently growing perturbations owing to the non-normal nature of the underlying linear stability operator. Transient amplification of perturbation energy is found for polynomial orders higher than zero, and a catalytic role of the continuous modes in increasing transient growth is demonstrated. The adjoint stability equations are derived and used in a numerical receptivity experiment to illustrate the scattering of vortical free-stream disturbances into the least stable boundary layer mode.

## 1. Introduction

For many shear flows stability results based on modal solutions are an essential part of describing and quantifying phenomena observed during the transition from laminar to turbulent fluid motion in shear flows. It is important, though, to keep in mind that modal solutions may merely describe the asymptotic stability of the flow and may fail to capture short-time disturbance growth. Only a non-modal stability analysis can reveal whether a specific flow type is dominated by modal (asymptotic) or non-modal (short-term) stability behaviour. The mathematical cause of non-modal behaviour is the non-normality of the underlying linear stability operator. Non-normal operators are defined as operators that do not commute with their associated adjoint operator; they have a set of non-orthogonal eigenfunctions that allow short-term growth of perturbation energy even in the presence of only damped eigenvalues (see Schmid & Henningson 2001).

Although the beginnings of stability theory based on the initial value problem (rather than the modal approach) can be traced back to Kelvin (1887) and Orr (1907), only more recent studies have stressed the importance of taking a non-modal approach to stability theory in a variety of shear flows. Short-term energy growth may provide the linear growth mechanism during transition to turbulence for subcritical parameter values. Applications to shear flows include, among others, pipe flow (Boberg & Brosa 1988; Bergström 1993; Schmid & Henningson 1994; Trefethen, Trefethen & Schmid 1999), plane channel and boundary layer flows (Butler & Farrell 1992; Reddy & Henningson 1993; Trefethen *et al.* 1993; Waleffe 1995; Corbett & Bottaro 2000), atmospheric boundary layers (Farrell 1989; Foster 1997), Taylor–Couette flow

† Present address: Cray Inc., Panamaweg 7, 5034 Suhr, Switzerland.

(Hristova *et al.* 2002; Meseguer 2001), granular flow (Schmid & Kytömaa 1994), stratified flow (Farrell & Ioannou 1993), and vortical flows (Schmid *et al.* 1993).

Having presented a detailed study of the spectrum of swept Hiemenz flow (see Part 1, Obrist & Schmid 2003) we now take the non-modal approach and investigate the stability operator in terms of its potential to support transiently growing solutions.

For a complete description of transition it is not sufficient to determine the stability behaviour, be it modal or non-modal. One also needs to address the issue of receptivity, i.e. the response of the flow to forcing, usually in the free stream outside the shear layer. Whereas stability studies concentrate on the evolution characteristics of homogeneous solutions to the linear evolution problem, receptivity studies address the evolution characteristics of the particular solution of the linear evolution problem stemming from specified forcing functions.

The field of receptivity studies is vast, often making use of advanced asymptotic methods (see Goldstein & Hultgren 1989 and references therein) or large-scale numerical simulations (for example, Jacobs & Henningson 1999). A rather concise and accurate method of studying the linear response behaviour involves the computation and analysis of the adjoint stability operator. The adjoint stability operator then allows us to address such topics as receptivity to wall roughness, free-stream sound, vibrating ribbons, or mass and momentum sources (see Hill 1995). Choosing this approach we will derive and analyse the adjoint stability operator for swept Hiemenz flow and conduct a simple but illustrative numerical receptivity experiment to verify and demonstrate the use of adjoint techniques in receptivity for swept attachment-line boundary layer flow.

## 2. Choice of disturbance measure

Non-modal stability analysis relies on the non-orthogonality of the eigenfunctions of the linear stability problem. Consequently, the way we measure the angle between the eigenfunctions, i.e. the way we define our inner product, is critical to the analysis of transient growth. Even though no one inner product is superior or more justifiable than any other, it is prudent to base the inner product on a physically meaningful norm. In temporal stability problems the kinetic disturbance energy is a quantity representative of the disturbance size. Furthermore, since the nonlinear terms of the Navier–Stokes equations preserve energy, it allows a clear decomposition into energy-generating and energy-preserving mechanisms. A different disturbance measure may not have this property.

For the case of swept Hiemenz flow we will start with a general norm based on the kinetic energy

$$e(t) = \iiint_D \rho(x, y, z)\tfrac{1}{2}[u'(x, y, z, t)^2 + v'(x, y, z, t)^2 + w'(x, y, z, t)^2]\,\mathrm{d}x\,\mathrm{d}y\,\mathrm{d}z, \quad (2.1)$$

where $\rho(x, y, z)$ is a weight function that is yet to be defined.

For the disturbance energy $e$ to be an applicable norm we must ensure that the integral in (2.1) exists. In general, the integration domain $D$ covers the entire flow field. In many canonical flow types, the flow field extends infinitely in at least one direction, and periodicity of the disturbances is often assumed in these coordinate directions. In this case we choose the weight function as $\rho(x, y, z) = 1$ for $-L_z/2 < z < L_z/2$ (and zero otherwise) for a periodic $z$-direction with $L_z$ denoting the length of one period.

We have to keep in mind that, although swept Hiemenz flow is an exact solution to the Navier–Stokes equations, it is a physically sensible solution only in the vicinity of the stagnation point, since the velocities grow without bounds as we move away from the stagnation point. It seems appropriate then to limit the chordwise domain of integration.

Motivated by the results from the analysis of the global stability problem (see Part 1) we choose the Hermite weight function $\exp(-x^2/2)$ to limit the extent of integration in the chordwise direction. The disturbance energy is thus given by

$$e(t) = \int_{-\infty}^{\infty} \mathrm{d}x \int_{0}^{\infty} \mathrm{d}y \int_{-L_z/2}^{L_z/2} \mathrm{d}z\, \mathrm{e}^{-x^2/2} \tfrac{1}{2}(u'(x,y,z,t)^2 + v'(x,y,z,t)^2 + w'(x,y,z,t)^2). \tag{2.2}$$

Using this weight function the integral in $x$ will exist, provided that the disturbance field does not grow faster than $\exp(x^2/4)$. In addition to that, the disturbance field must decay faster than $y^{-1/2}$ as $y \to \infty$. Basing the inner product and norm on this disturbance energy thus yields

$$\|(u', v', w')\| \equiv e^{1/2}. \tag{2.3}$$

We then use a Fourier–Hermite expansion

$$\begin{pmatrix} u'(x,y,z,t) \\ v'(x,y,z,t) \\ w'(x,y,z,t) \end{pmatrix} = \sum_{m=-\infty}^{\infty} \sum_{n=0}^{\infty} \begin{pmatrix} \tilde{u}_{mn}(y,t) \\ \tilde{v}_{mn}(y,t) \\ \tilde{w}_{mn}(y,t) \end{pmatrix} \mathrm{He}_n(x) \mathrm{e}^{\mathrm{i}\beta_m z}, \tag{2.4}$$

where $\mathrm{He}_n(x)$ are normalized Hermite polynomials, to decompose the disturbance field $(u', v', w')$. Using this expansion, the orthogonality relation of Hermite polynomials, and Parseval's identity, we can define the following energy density:

$$e_{mn} = \int_{0}^{\infty} \tfrac{1}{2}\left(\tilde{u}^*_{mn}\tilde{u}_{mn} + \tilde{v}^*_{m(n-1)}\tilde{v}_{m(n-1)} + \tilde{w}^*_{m(n-1)}\tilde{w}_{m(n-1)}\right) \mathrm{d}y. \tag{2.5}$$

The energy density $e_{mn}$ corresponds to the Hermite polynomial of order $n$ for the $m$th spanwise Fourier mode of the chordwise velocity $u'$, but only to the Hermite polynomial of order $n-1$ for $v'$ and $w'$. For the case $n = 0$ the terms containing $\tilde{v}$ and $\tilde{w}$ vanish. This is consistent with the results from the analysis of the global stability problem, where we found that the polynomial degree describing a given eigenfunction is one order lower for $v$ and $w$ than for $u$.

Although this definition of the energy norm has several advantageous properties, one has to keep in mind that our choice of the Hermite weight function $\rho(x) = \exp(-x^2/2)$ is still somewhat arbitrary. The super-exponential decay of $\rho(x)$ for large $|x|$ results in the under-representation of disturbance structures far from the stagnation point. Only disturbances close to the stagnation point will contribute significantly to the disturbance energy.

We propose a generalization of the chordwise integration weight to $\exp[-(x/\gamma)^2/2]$. The parameter $\gamma$ determines the extent of the weight function in the chordwise direction. A larger value of $\gamma$ will account for disturbances farther from the stagnation point. For $\gamma = 1$ we recover the previous weight function. We define

$$e^{(\gamma)} = \int_{-\infty}^{\infty} \mathrm{d}x \int_{0}^{\infty} \mathrm{d}y \int_{-L_z/2}^{L_z/2} \mathrm{d}z\, \mathrm{e}^{-(x/\gamma)^2/2} \tfrac{1}{2}(u'^2 + v'^2 + w'^2). \tag{2.6}$$

To define a generalized energy density we have to reformulate the Hermite expansion in terms of the stretched variable $x/\gamma$,

$$\begin{pmatrix} u'(x,y,z,t) \\ v'(x,y,z,t) \\ w'(x,y,z,t) \end{pmatrix} = \sum_{m=-\infty}^{\infty} \sum_{n=0}^{\infty} \begin{pmatrix} \tilde{u}_{mn}^{(\gamma)}(y,t) \\ \tilde{v}_{mn}^{(\gamma)}(y,t) \\ \tilde{w}_{mn}^{(\gamma)}(y,t) \end{pmatrix} \mathrm{He}_n(x/\gamma) \mathrm{e}^{\mathrm{i}\beta_m z}. \tag{2.7}$$

This allows us to write the generalized form of the energy density as

$$e_{mn}^{(\gamma)} = \int_0^{\infty} \tfrac{1}{2} \left( \tilde{u}_{mn}^{(\gamma)*} \tilde{u}_{mn}^{(\gamma)} + \tilde{v}_{m(n-1)}^{(\gamma)*} \tilde{v}_{m(n-1)}^{(\gamma)} + \tilde{w}_{m(n-1)}^{(\gamma)*} \tilde{w}_{m(n-1)}^{(\gamma)} \right) \mathrm{d}y. \tag{2.8}$$

The coefficients with respect to the stretched chordwise variable $(\tilde{u}_{mn}^{(\gamma)}, \tilde{v}_{mn}^{(\gamma)}, \tilde{w}_{mn}^{(\gamma)})$ can easily be computed from the original coefficients $(\tilde{u}_{mn}, \tilde{v}_{mn}, \tilde{w}_{mn})$.

We will see later that a combination of disturbance measures based on several values of $\gamma$ provides a more complete picture of the disturbance dynamics for swept Hiemenz flow. If not otherwise stated we will use $\gamma = 1$ in what follows.

## 3. Non-modal analysis

After having defined an energy norm upon which to base our non-modal analysis, we will briefly outline the steps involved in the quantitative description of transient behaviour. Full details and extensions of this procedure are given in Schmid & Henningson (2001) and Obrist (2000).

Given a linear initial value problem of the form

$$\dot{\boldsymbol{q}} = \boldsymbol{A}\boldsymbol{q}, \quad \boldsymbol{q}(0) = \boldsymbol{q}_0,$$

the general solution can be written formally as

$$\boldsymbol{q} = \mathrm{e}^{t\boldsymbol{A}} \boldsymbol{q}_0. \tag{3.1}$$

An eigenvalue decomposition will diagonalize $\boldsymbol{A}$ (assuming non-degenerate eigenvalues) according to

$$\boldsymbol{A} = (\tilde{\boldsymbol{q}}_1 | \cdots | \tilde{\boldsymbol{q}}_j | \cdots) \begin{pmatrix} -\mathrm{i}\beta c_1 & & & \\ & \ddots & & \\ & & -\mathrm{i}\beta c_j & \\ & & & \ddots \end{pmatrix} (\tilde{\boldsymbol{q}}_1 | \cdots | \tilde{\boldsymbol{q}}_j | \cdots)^{-1} \tag{3.2}$$

where $\tilde{\boldsymbol{q}}_j$ are the eigenvectors corresponding to the eigenvalues $c_j$.

This allows us to rewrite (3.1) as

$$\boldsymbol{q} = (\tilde{\boldsymbol{q}}_1 | \cdots | \tilde{\boldsymbol{q}}_j | \cdots) \begin{pmatrix} \mathrm{e}^{-\mathrm{i}\beta c_1 t} & & & \\ & \ddots & & \\ & & \mathrm{e}^{-\mathrm{i}\beta c_j t} & \\ & & & \ddots \end{pmatrix} (\tilde{\boldsymbol{q}}_1 | \cdots | \tilde{\boldsymbol{q}}_j | \cdots)^{-1} \boldsymbol{q}_0. \tag{3.3}$$

Modal analysis is concerned with the diagonal operator containing the eigenvalues $\{-\mathrm{i}\beta c_1, \ldots, -\mathrm{i}\beta c_j, \ldots\}$, neglecting the form of the transformation operator that resulted in a diagonalized operator. If the operator $\boldsymbol{A}$ is normal, the eigenfunctions $\tilde{\boldsymbol{q}}_j$ form an orthogonal basis and the dynamics of $\boldsymbol{q}$ is governed for all times by the

eigenvalues, i.e. exponential growth if there is at least one eigenvalue with $\mathrm{Im}(c_j) > 0$ and exponential decay otherwise. If the operator $\boldsymbol{A}$ is non-normal, on the other hand, the eigenfunctions $\tilde{\boldsymbol{q}}_j$ are non-orthogonal and the eigenvalues only describe the asymptotic behaviour as $t \to \infty$. On a short time scale, transient growth is possible as a result of the non-orthogonal superposition of exponential solutions. This is true even in the presence of only damped modes. To analyse the short-term behaviour of non-normal operators, both eigenvalues and eigenfunctions have to be taken into account. The linear stability operator for swept Hiemenz flow is non-normal and requires such an analysis.

We start by defining the optimal amplification, $G(t)$, of energy at a given time $t$ as the ratio of the norm of a disturbance at time $t$ to its initial norm, maximized over all possible initial conditions. We obtain

$$G(t) = \sup_{\boldsymbol{q}_0} \frac{\|\boldsymbol{q}(t)\|^2}{\|\boldsymbol{q}_0\|^2}.$$

Using our formal solution of the initial value problem (3.1) we obtain

$$G(t) = \sup_{\boldsymbol{q}_0} \frac{\|\mathrm{e}^{\boldsymbol{A}t}\boldsymbol{q}_0\|^2}{\|\boldsymbol{q}_0\|^2} = \|\mathrm{e}^{\boldsymbol{A}t}\|^2.$$

The quantity $G(t)$ describes the maximum energy any normalized initial condition can achieve at time $t$. As time evolves, all disturbances will eventually decay if no unstable eigenvalues are present. We are thus interested in the maximum $G(t)$ over time, i.e.

$$G_{\max} = \max_{t>0} G(t). \tag{3.4}$$

When evaluating the norm of $\mathrm{e}^{t\boldsymbol{A}}$ we should recall that it is the energy norm (2.3) we are interested in. Computationally, this is accomplished by introducing weight matrices that convert the energy norm defined in (2.2) to a standard 2-norm which is easily computed using a singular value decomposition (SVD). Details of this procedure can be found in Schmid & Henningson (2001) and Obrist (2000).

In the next section we will present results from computing the maximum amplification $G(t)$ for swept Hiemenz flow. We will investigate the reduced operator $\tilde{\boldsymbol{A}}$ by including only a finite number of selected eigenfunctions in (3.2):

$$\begin{aligned}\tilde{\boldsymbol{A}} &= (\tilde{\boldsymbol{q}}_1|\cdots|\tilde{\boldsymbol{q}}_N)\begin{pmatrix} -\mathrm{i}\beta c_1 & & \\ & \ddots & \\ & & -\mathrm{i}\beta c_N \end{pmatrix}(\tilde{\boldsymbol{q}}_1|\cdots|\tilde{\boldsymbol{q}}_N)^{-1} \\ &= \tilde{\boldsymbol{Q}}\tilde{\boldsymbol{\Lambda}}\tilde{\boldsymbol{Q}}^{-1}.\end{aligned}$$

In this way we are able to analyse uniform, Görtler–Hämmerlin and higher-order modes for their potential to support transiently growing solutions, and to investigate the effects of the continuous spectrum (algebraically decaying modes) on the non-modal dynamics of disturbances.

## 4. Transient growth for swept Hiemenz flow

After the brief description of non-modal stability analysis in the previous section, we now present applications of this methodology to swept Hiemenz flow. We base our calculations on the eigensolutions of the global stability problem (see Part 1).

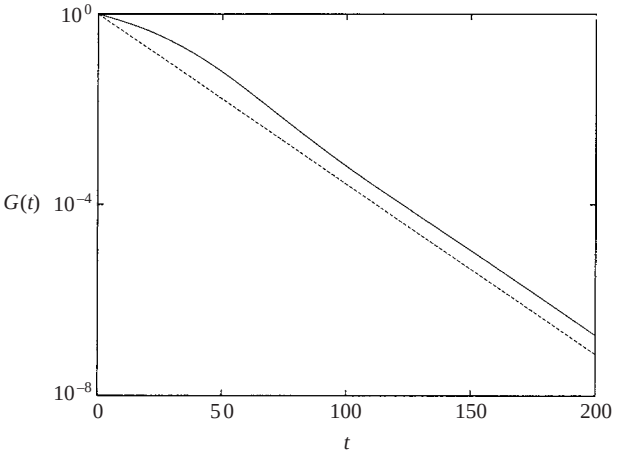


FIGURE 1. Optimal energy $G(t)$ for $Re = 550$ and $\beta = 0.25$ obtained with discrete uniform modes; the dashed line shows the rate of decay of the least stable mode.

We will systematically study transient growth phenomena by choosing eigensolutions up to a given order of the chordwise polynomial. Furthermore, we will distinguish between discrete (exponentially decaying) and continuous (algebraically decaying) modes. Both even and odd modes will be discussed (which can be studied separately, since they are orthogonal under any inner product that preserves the chordwise symmetry).

### 4.1. *Discrete uniform modes*

We begin by restricting the basis $\tilde{\boldsymbol{Q}}$ of eigenvectors to the discrete uniform modes (see Part 1) and recall that these modes consist only of chordwise velocity disturbances $\hat{u}$ that are independent of $x$.

The optimal energy amplification $G(t)$ (figure 1) shows that there is a very small non-modal effect resulting in the delay of the asymptotic energy decay. No amplification beyond the initial energy is observed.

### 4.2. *Discrete Görtler–Hämmerlin modes*

When including modes from the upper, lower, and uniform branches of the Görtler–Hämmerlin spectrum (see Part 1) in the basis of the non-modal analysis, we obtain — for $Re = 550$ and $\beta = 0.25$ — the results displayed in figure 2.

At $t \approx 70$ the initial energy is amplified approximately eight times, after which the energy begins to decay exponentially. The rate of decay asymptotically approaches the rate of decay of the least stable mode $(c_r, c_i) = (0.3755037, -0.0033626)$. At this point, all modes, except for the least stable one, have decayed. An equivalent modal initial condition would have to start with an initial energy of about nine times the modal one to exhibit the same asymptotic behaviour. The dashed line in figure 2 ($a$) represents the temporal evolution of energy for this modal initial condition. By exploiting the non-modal growth mechanism one can achieve higher energies more efficiently.

To validate the theoretical results above we use the initial condition resulting in the largest energy $G_{\max}$, which we find at $t \approx 70$, in a direct numerical simulation (DNS) (see Obrist (2000) for a detailed description of the numerical method). We choose a very small amplitude for the initial condition to comply with linear theory. The grid consists of $192 \times 97 \times 16$ points, a dissipative fringe region covers 30 chordwise points,

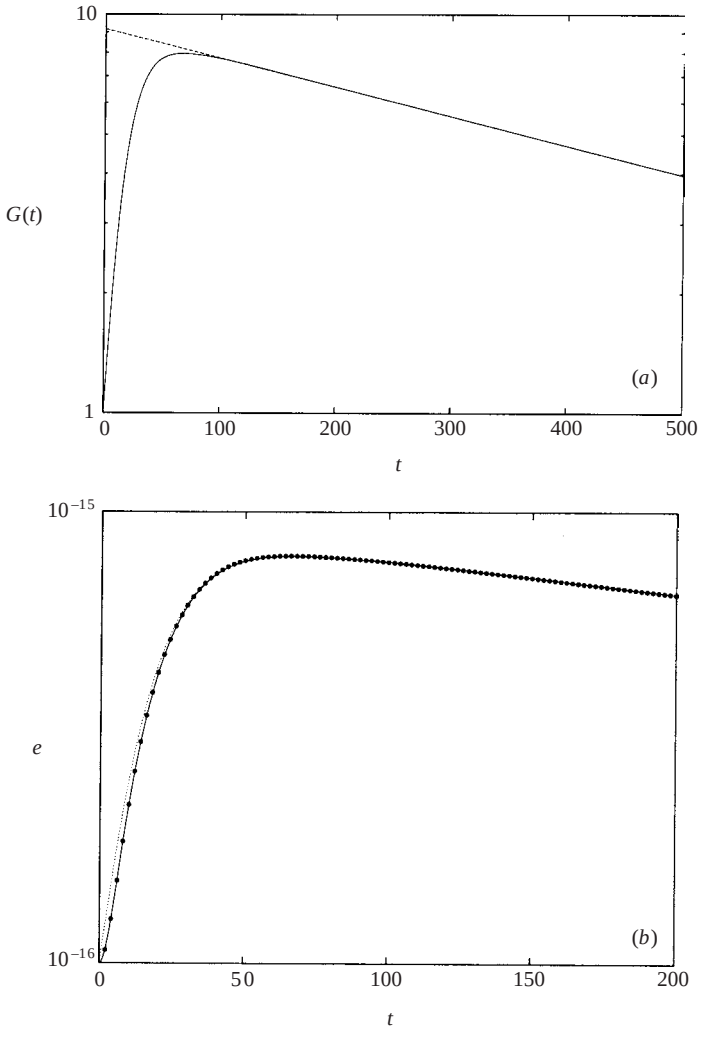


FIGURE 2. (*a*) Optimal energy $G(t)$ for $Re = 550$ and $\beta = 0.25$ obtained with discrete Görtler–Hämmerlin modes; the dashed curve shows the decay of a single least stable mode given an initial energy that matches the energy level of $G(t)$ asymptotically as $t \to \infty$. (*b*) Disturbance energy $e$ for optimal initial conditions at $Re = 550$ and $\beta = 0.25$ (——, linear theory; ●, DNS); the thin dotted line shows $10^{-16} \times G(t)$.

and the computational domain spans $[-150, 150] \times [0, 500] \times [-4\pi, 4\pi]$ with half the grid points in the $y$-direction clustered in the interval $[0, 4]$.

The disturbance energy resulting from the simulation is shown by symbols in figure 2(*b*); the theoretical result is added as a solid line. The agreement between theory and numerical experiment is very good. The energy curve from the numerical simulations touches the theoretical curve $G(t)$ at its maximum, since $G(t)$ is an envelope over all unit energy initial conditions, whereas the numerical results represent the evolution of a specific initial condition.

The maximum energy amplification $G_{\max}$ is about 8 for $Re = 550$ and $\beta = 0.25$. By varying the Reynolds number $Re$ and the spanwise wavenumber $\beta$ we obtain figure 3 which shows contours of $G_{\max}$. The point ($Re = 550$, $\beta = 0.25$) is indicated by

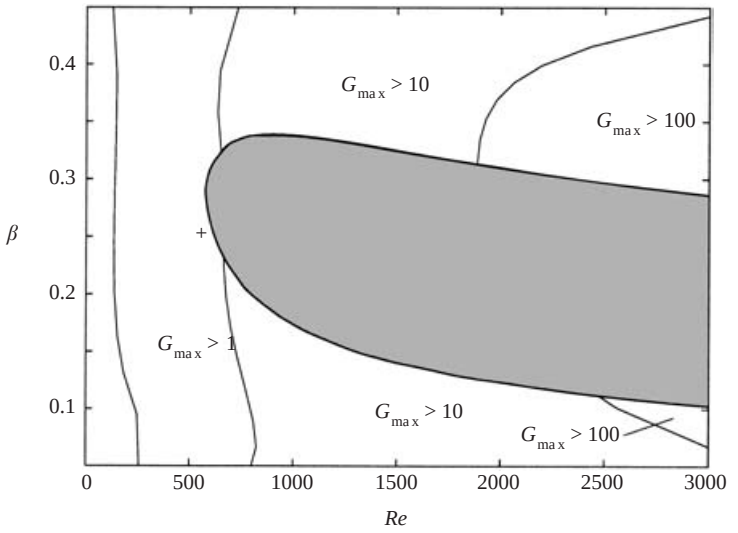


FIGURE 3. Maximal energy amplification $G_{\max}$ obtained from discrete Görtler–Hämmerlin modes as a function of $Re$ and $\beta$. The symbol + indicates the parameter values $Re = 550$ and $\beta = 0.25$ used in the transient growth computations.

a symbol. The shaded area signifies a linearly unstable flow, and the maximal energy amplification is therefore infinite for these parameter combinations. The potential for transient growth is bigger for larger Reynolds numbers. For $Re < 200$ transient growth disappears. Within the range examined the maximum energy amplification depends only weakly on the spanwise wavenumber $\beta$. Only for large Reynolds numbers do we observe a substantial influence of $\beta$ on $G_{\max}$.

### 4.3. *Discrete higher-order modes*

Figure 4 (*a–c*) shows direct numerical simulation results for optimal initial conditions chosen from subsets of discrete modes up to polynomial order $N = 2$, 3, and 4, respectively. The disturbance energies of the DNS results are split into energy densities as defined by (2.5). Again, we note a nearly perfect match with the theoretical results. Most of the energy is propagated by the lowest-order energy density, that is, the energy density $e_0$ for even modes and $e_1$ for odd modes. On the other hand, the highest-order energy densities hardly exhibit any transient growth of their own.

Although this last observation may suggest that higher-order modes do not create significant transient growth, the opposite is true: higher-order modes are crucial to a strong transient growth. To document this fact we computed $G(t)$ for the discrete modes at $Re = 1000$, $\beta = 0.4$, where we allowed increasingly higher polynomial orders $N$. We see in figure 5 that transient growth becomes stronger with increasing polynomial order.

In Part 1 we made the observation that modes of different polynomial order but equal rank within the spectrum have very similar eigenfunctions. For example, the least-stable mode for $N \leqslant 1$ and the least-stable mode for $N \leqslant 3$ show nearly the same eigenfunction when comparing the components $\hat{v}_0$ and $\hat{u}_1$. The eigenfunctions only differ substantially in that the least-stable mode for $N \leqslant 3$ additionally contains the components $\hat{v}_2$ and $\hat{u}_3$, which do not exist for $N \leqslant 1$. The resemblance of the eigenfunctions for different polynomial order is the source of strong transient growth, and as we include higher orders in our subset we include more eigenfunctions that

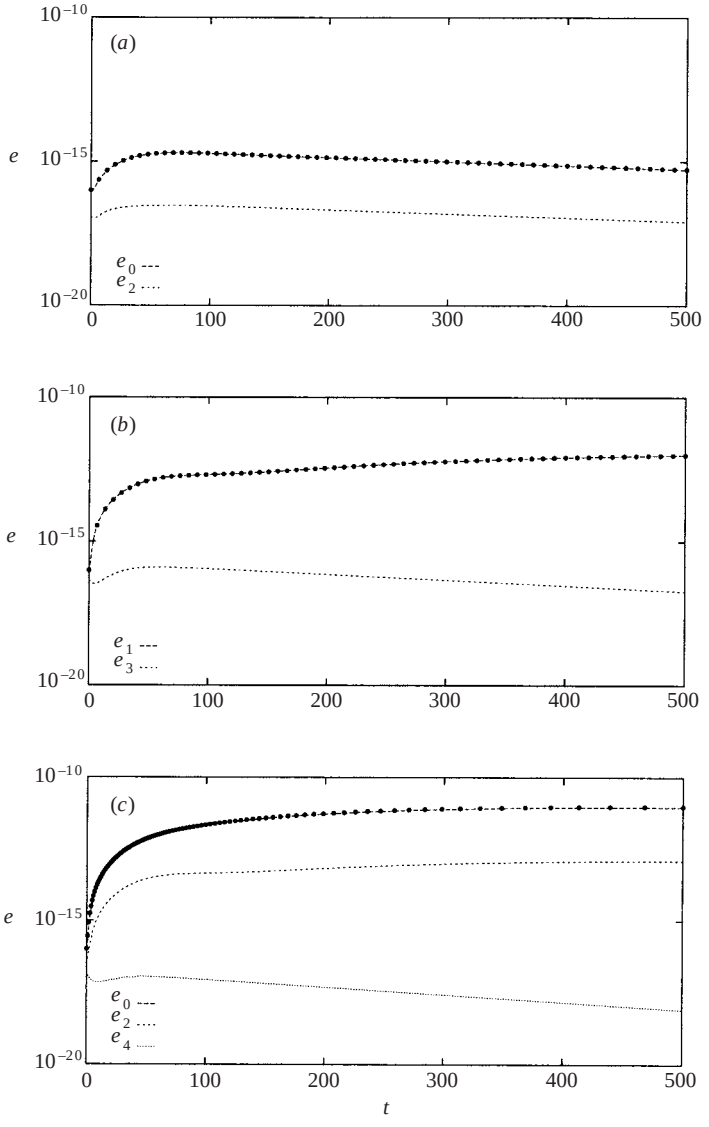


FIGURE 4. Energy densities $e_i$ for optimal initial conditions at $Re = 550$, $\beta = 0.25$ chosen from subsets limited by (*a*) $N \leqslant 2$, (*b*) $N \leqslant 3$, (*c*) $N \leqslant 4$; the dots show the disturbance energy $e$ as predicted by the linear theory.

are nearly parallel to each other. We hence introduce more degrees of freedom to construct an initial condition that consists of mutually cancelling modal solutions, thereby increasing the potential for transient growth.

The results suggest that arbitrarily high energy amplifications can be reached if only modes of high enough polynomial orders are allowed. This conclusion, however, does not acknowledge the fact that the linearization of the Navier–Stokes equations is only valid for very small disturbance amplitudes. In Part 1 we derived a condition for the validity of the linear modes and found that for increasing polynomial order increasingly severe restrictions on the amplitude of the modal solutions have to be imposed. These restrictions oppose the seemingly unbounded increase in energy for

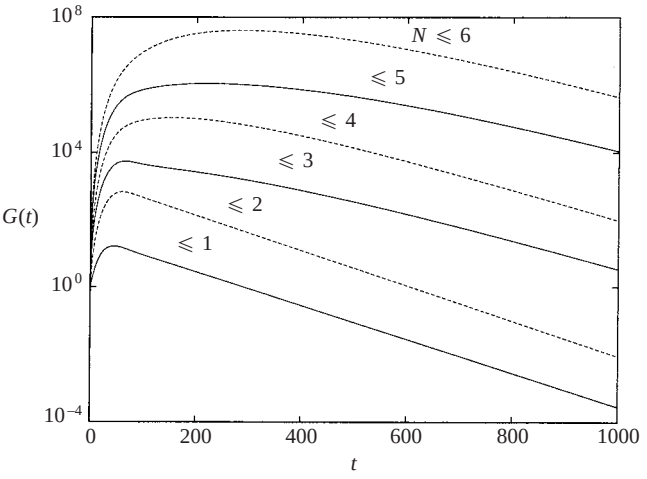


FIGURE 5. Optimal energy $G(t)$ at $Re = 1000$, $\beta = 0.4$ for subsets of discrete modes limited to polynomial orders $N \leqslant 1, \ldots, 6$; solid lines show the odd transients and dashed lines show the even transients.

higher polynomial orders. There will be a limit to the attainable energy, and this limit is due to the breakdown of our assumptions that resulted in the linear global stability problem.

### 4.4. *Algebraically decaying modes*

Before we can proceed to study optimal initial conditions constructed with modes that decay algebraically in $y$ we have to modify our energy norm. In § 2 we found that the disturbance field has to decay faster than $y^{-1/2}$ as $y \to \infty$ for the integral in (2.2) to exist. We are now faced with the problem that in some cases the algebraically decaying modes do not decay sufficiently fast. We resolve this issue by changing the upper limit of integration in the energy norm to $y_{\max} = 500$.

We find that restricting our subset to algebraically decaying modes yields transient growth which is weaker than can be obtained with discrete modes only. In combination with discrete modes, however, we obtain very strong transient growth. For instance, the two subsets $A$ (discrete modes) and $B$ (continuous, algebraically decaying modes) for $Re = 550$, $\beta = 0.25$, and $N \leqslant 4$ (as defined in figure 6) result in the three optimal energy curves that are generated from (i) the subset $A$, (ii) the subset $B$, and (iii) the union of $A$ and $B$ as displayed in figure 7.

We support these results with a numerical simulation of optimal initial conditions created from both discrete and continuous modes for $Re = 550$, $\beta = 0.25$, and $N \leqslant 2$ (figure 8). Again, the energy amplification is about two orders of magnitude stronger than for initial conditions based on discrete modes only. This leads us to the conclusion that algebraically decaying modes enhance transient growth but cannot produce strong transient growth on their own; they exert a strong catalytic effect on the discrete modes.

### 4.5. *Upstream energy transport and suboptimal disturbances*

Let us revisit the numerical experiment in § 4.2 where we created an optimal initial condition based on discrete Görtler–Hämmerlin modes. The initial condition was optimal with respect to the energy norm (2.6) with $\gamma = 1$. We repeat the numerical simulation with the same initial condition, but this time we also measure the energy

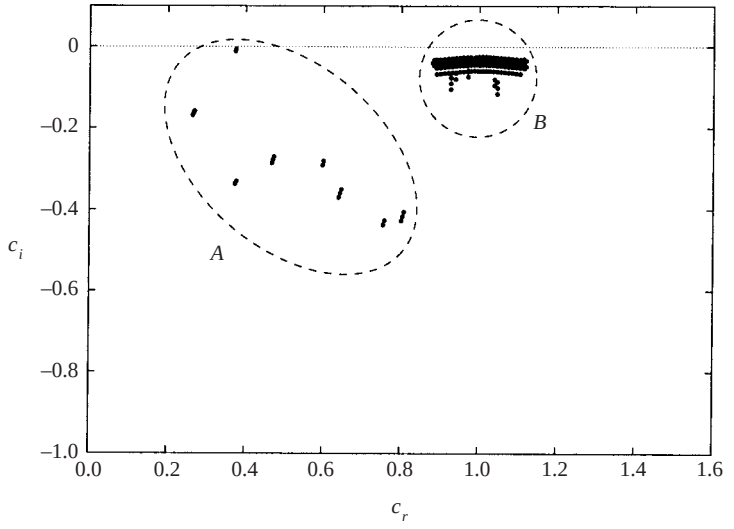


FIGURE 6. Definition of the subsets $A$ and $B$ for $Re = 550$, $\beta = 0.25$, and $N \leqslant 4$.

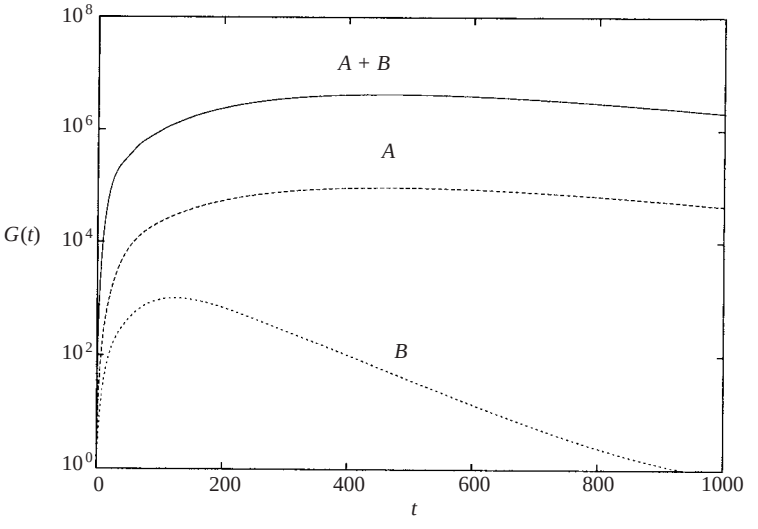


FIGURE 7. Optimal energy $G(t)$ obtained for the subsets $A$, $B$, and the union of $A$ and $B$ ($Re = 550$, $\beta = 0.25$, $N \leqslant 4$).

norm $e^{(50)}$ ($\gamma = 50$), which we shall call the *outer energy* — as opposed to the *inner energy* $e^{(1)}$. Figure 9 displays both energies versus time. We observe transient effects for both energy norms. The outer energy, however, decays rapidly in this transient phase, whereas the inner energy increases up to its optimal point. Increasing the parameter $\gamma$ alters the weight function by widening the Gaussian in (2.6); see figure 10. Thus the energy norm takes into account information from a larger chordwise interval. For a small $\gamma$ only information close to the stagnation point enters the norm. Therefore disturbances farther from the stagnation point contribute only to $e^{(50)}$. Disturbances near the stagnation point contribute to both $e^{(1)}$ and $e^{(50)}$. The difference between the

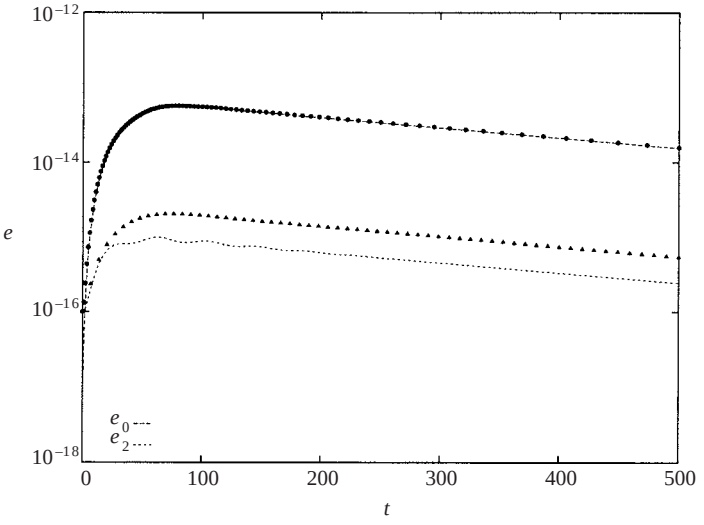


FIGURE 8. Energy densities $e_i$ for optimal initial conditions at $Re = 550$ and $\beta = 0.25$ chosen from a subset of discrete and algebraically decaying modes up to $N = 2$; the dots show the disturbance energy $e$ as predicted by the linear theory, the triangles show the evolution of the optimal initial conditions made up of discrete modes only.

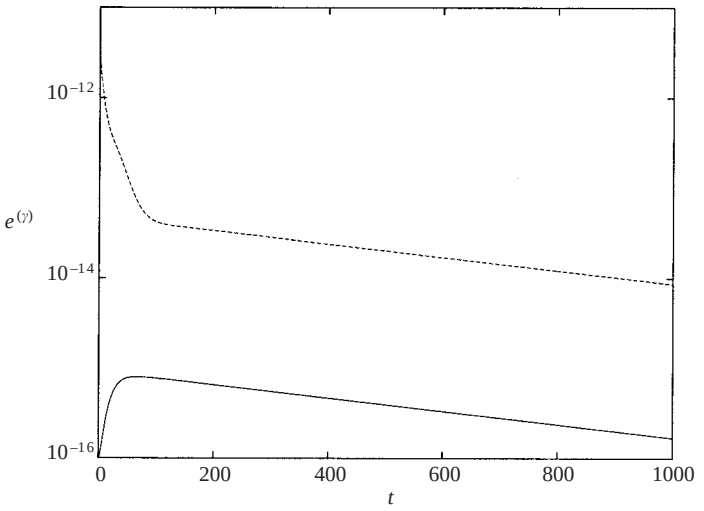


FIGURE 9. Inner and outer energies $e^{(1)}$ and $e^{(50)}$ for optimal initial conditions at $Re = 550$ and $\beta = 0.25$ (——, $e^{(1)}$; – – –, $e^{(50)}$).

two energies reflects disturbances that are contained in the outer energy but are far enough from the stagnation point to not be accounted for in the inner energy.

With this in mind, we interpret figure 9 as follows. An optimal initial condition using $\gamma = 1$ has minimal energy close to the stagnation point. There may be a significant amount of energy farther from the stagnation point, but this energy is not reflected by $e^{(1)}$ but rather by $e^{(50)}$ — hence the large difference in energy at $t = 0$. As the flow evolves we obtain the expected transient growth in the inner energy. At the same time the outer energy decays rapidly. As a result the difference between

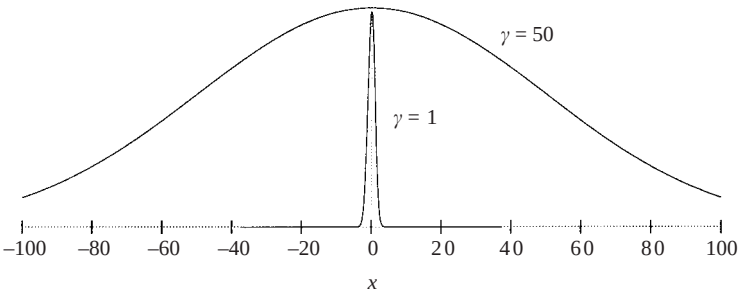


FIGURE 10. Weight functions for the inner and outer energies $e^{(1)}$ and $e^{(50)}$.

the two energies decays at an even higher rate. Consequently, energy must have been transported upstream along the chordwise axis toward the stagnation point. In a recent study, Türkyilmazoğlu & Gajjar (1999) — using techniques explained in Huerre & Monkewitz (1990) — showed that Hiemenz flow is susceptible to an absolute instability in the chordwise direction which confirms the observation of energy propagation toward the stagnation point.

Suboptimal initial conditions are defined as initial conditions that show a substantial amount of transient growth but are not obtained by a singular value decomposition of the evolution operator. For channel flow, Gustavsson (1991) suggested taking a vector eigenfunction of the Orr–Sommerfeld equation and deleting the wall-normal vorticity fluctuations, which is equivalent to a superposition of the original vector eigenfunction with Squire modes (consisting of vorticity fluctuations only) such that the wall-normal vorticity cancels.

We will employ a similar technique to obtain a large (but sub-optimal) amount of energy amplification for swept Hiemenz flow. We found that disturbances far from the stagnation point ($|x| \gg \gamma$) are not accounted for in the energy $e^{(\gamma)}$. This observation suggests that a sub-optimal initial condition should have small amplitudes close to the stagnation point, but may have large amplitudes as $|x| \to \infty$: monomials $x^N$ of large order $N$ satisfy these requirements. To construct an initial condition that is a monomial in $x$ we take, say, the least-stable mode of order $N$ (which is generally a full polynomial) and neglect all lower-order terms. This is equivalent to a superposition of the least-stable mode of order $N$ with modes of orders $N-2$, $N-4$, ..., such that the lower-order terms of the least-stable mode are cancelled out. Generating such an initial condition is computationally very simple; nevertheless, the temporal evolution of its eigenfunction components gives rise to significant transient growth in energy.

To illustrate the concept of sub-optimal initial conditions, we take the least-stable mode of order $N = 4$ and retain only the monomial term of order 4. Figure 11 shows the results of a direct numerical simulation starting with this sub-optimal initial condition. As the flow evolves $e_4$, the highest-order energy density, decays exponentially with the decay rate of the least-stable mode of order 4. The two lower-order energies $e_0$ and $e_2$, however, exhibit strong transient growth. The total disturbance energy $e$ is amplified by six orders of magnitude in this example. We notice that this amount of amplification is comparable to the optimal energy $G(t)$ that can be achieved by combining modes from the subsets $A$ and $B$ from figure 6. Furthermore, the amplification of the sub-optimal initial condition is considerably stronger than the amplification we could obtain from the discrete modes only.

Clearly, other techniques to generate sub-optimal initial conditions are conceivable; yet, the simple method above presents an efficient way to generate initial conditions

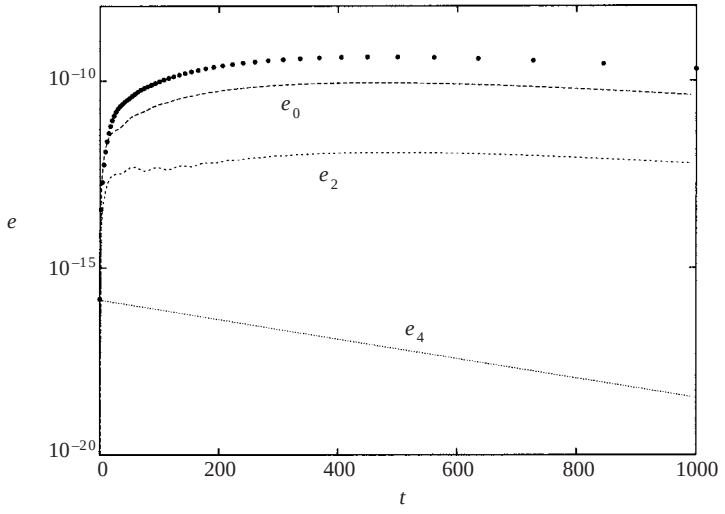


FIGURE 11. Energy densities $e_i$ for a sub-optimal initial condition with $N = 4$ at $Re = 550$, $\beta = 0.25$; the dots show the optimal energy $G(t)$ obtained from the union of subsets $A$ and $B$ from figure 6.

that show strong transient growth. This type of initial condition could be used in numerical simulations that seek to trigger turbulent fluid motion in a simple but highly efficient manner.

## 5. Adjoint stability equations for swept Hiemenz flow

Receptivity describes the process by which external disturbances (such as, e.g., acoustical waves, free-stream turbulence or wall roughness) interact with and generate disturbances in the boundary layer. It is a fundamental process that should be considered an integral part of a stability analysis as it provides a seeding mechanism for linear instabilities in shear layers. Receptivity can be studied in a variety of ways, ranging from matched asymptotics (see Goldstein & Hultgren 1989) to perturbation analysis (Crouch 1992*a*, *b*; Choudhari 1996). A relatively new method to address the receptivity problem is based on the adjoint stability equations (Hill 1995; Luchini & Bottaro 1998) where the adjoint variables are used to quantify the projection of external disturbance fields onto boundary layer modes. Due to its elegance, we will pursue this particular approach to receptivity in this manuscript.

An exhaustive study of receptivity for the case of swept Hiemenz flow is beyond the scope of this paper. We will provide, however, the relevant equations and mathematical framework to conduct investigations of the response of swept Hiemenz flow to external perturbations. A numerical receptivity experiment will demonstrate the validity and efficiency of the approach presented.

The operator $\mathscr{K}^+$ which is adjoint to the operator $\mathscr{K}$ is defined by the relation

$$(p, \mathscr{K} q) = (\mathscr{K}^+ p,\ q), \tag{5.1}$$

with $(\cdot, \cdot)$ as an appropriately chosen inner product. In the case of a matrix $\boldsymbol{K}$, the associated adjoint operator $\boldsymbol{K}^+$ is simply the Hermitian $\boldsymbol{K}^H$.

For the generalized eigenvalue problem with eigenvalue $c$ and eigenfunction $q$,

$$\mathscr{K} q = c \mathscr{L} q, \tag{5.2}$$

the adjoint eigenvalue problem is defined as

$$\mathscr{K}^{+}q^{+} = \mu\mathscr{L}^{+}q^{+}. \tag{5.3}$$

The eigenvalues $\mu$ are the complex conjugates of the eigenvalues $c$, and the bi-orthogonality relation between the eigenfunctions $q$ and their adjoints $q^{+}$ can easily be derived as

$$(q_m^{+}, \mathscr{L}q_n) = \delta_{mn}. \tag{5.4}$$

We will later use the adjoint eigenfunctions $q_n^{+}$ to find the coefficients of the eigenfunction expansion of functions $f$ that lie within the space spanned by a finite number of regular eigenfunctions $q_n$, that is

$$f = \sum_{n=0}^{\infty} \tilde{a}_n q_n. \tag{5.5}$$

The coefficients $\tilde{a}_n$ are given as

$$\tilde{a}_m = (q_m^{+}, \mathscr{L}f). \tag{5.6}$$

For our receptivity study we will use the above technique to find how strongly a specific mode (e.g. the most unstable mode) is excited by an initial condition $f$.

We then need to derive and solve the eigenvalue problem that is adjoint to the original global stability problem (see Part 1). We will see that the derivation of the adjoint operators, which typically involves repeated integration by parts for all independent variables accounted for in the scalar product, can be substantially simplified by using the Hermite expansion of the global stability problem. In addition to the derivation of the adjoint operators we make an appropriate choice for the boundary conditions of the adjoint problem.

We choose an inner product based on the energy metric (2.5) and define

$$(p, q)_{\tilde{H}} \equiv \int_{-\infty}^{\infty}\int_{0}^{\infty} \mathrm{e}^{-x^2/2} p^H q \,\mathrm{d}x\,\mathrm{d}y. \tag{5.7}$$

We take $p$ and $q$ as the vectors $(\hat{u}, \hat{v})^T$, consisting of the chordwise and normal velocity components.

### 5.1. *Treatment of the chordwise direction*

In the chordwise direction we have to take into account the Hermite weight function $\exp(-x^2/2)$ when deriving the operators adjoint to chordwise differentiation. Boundary conditions do not need to be enforced explicitly as long as we restrict our solution space to functions for which the norm $\|q\|_{\tilde{H}} \equiv (q, q)_{\tilde{H}}^{1/2}$ exists, i.e. to functions that do not grow faster than $\exp(x^2/4)$ as $|x|$ tends to infinity.

As an example we derive the operator adjoint to the chordwise differentiation $\partial_x$ under the Hermite inner product,

$$\begin{aligned}(p, \partial_x q)_{\tilde{H}} &= \int_{-\infty}^{\infty}\int_{0}^{\infty} \mathrm{e}^{-x^2/2} p^H \partial_x q \,\mathrm{d}x\,\mathrm{d}y \\ &= \mathrm{e}^{-x^2/2} p^H q\Big|_{-\infty}^{\infty} + \int_{-\infty}^{\infty}\int_{0}^{\infty} \mathrm{e}^{-x^2/2}\,[x - \partial_x]\, p^H q \,\mathrm{d}x\,\mathrm{d}y \\ &= ([x - \partial_x]\, p, q)_{\tilde{H}},\end{aligned}$$

which yields

$$(\partial_x)^{+} = (x - \partial_x).$$

For more complicated operators the derivation of the adjoint operator quickly becomes unwieldy. It is helpful at this point to again take advantage of the Hermite expansion of the dependent variables in the chordwise coordinate direction that was introduced in Part 1 to separate the global eigenvalue problem.

The dependent variables are expanded in a series of normalized Hermite polynomials $\mathrm{He}_n(x)$,

$$p(x, y) = \sum_{n=0}^{N-1} \tilde{p}_n(y)\,\mathrm{He}_n(x). \tag{5.8}$$

and the series is truncated after $N$ terms.

Under this expansion the global stability problem transforms into a matrix eigenvalue problem whose coefficients contain wall-normal differential operators $\partial_y$. The Hermite expansion then allows us to rewrite the inner product (5.7) as

$$(p, q)_{\tilde{H}} = \int_0^\infty \mathbf{p}^H \boldsymbol{q}\,\mathrm{d}y,$$

where $\mathbf{p}$ and $\boldsymbol{q}$ denote the vectors of coefficients $\tilde{p}_n(y)$, $\tilde{q}_n(y)$. Returning to the above example, the first derivative of $p(x, y)$ can be represented as

$$\begin{aligned}\partial_x p &= \sum_{n=0}^{N-1} \tilde{p}_n(y)\partial_x \mathrm{He}_n(x)\\ &= \sum_{n=1}^{N-1} \tilde{p}_n(y)\sqrt{n}\mathrm{He}_{n-1}(x)\\ &= \sum_{n=0}^{N-2} \tilde{p}_{n+1}(y)\sqrt{n+1}\mathrm{He}_n(x),\end{aligned}$$

which can also be expressed by the matrix operator $\boldsymbol{D}$,

$$\boldsymbol{D} = \begin{pmatrix} 0 & \sqrt{1} & & & \\ & 0 & \sqrt{2} & & \\ & & \ddots & \ddots & \\ & & & 0 & \sqrt{N-1} \\ & & & & 0 \end{pmatrix},$$

such that

$$\partial_x q \longleftrightarrow \boldsymbol{D}\boldsymbol{q}.$$

It then follows from

$$(p, \partial_x q)_{\tilde{H}} = \int_0^\infty \mathbf{p}^H \boldsymbol{D}\boldsymbol{q}\,\mathrm{d}y = \int_0^\infty (\boldsymbol{D}^H \mathbf{p})^H \boldsymbol{q}\,\mathrm{d}y = ([x - \partial_x]\,p, q)_{\tilde{H}},$$

that the adjoint operator $x - \partial_x$ corresponds to the matrix operator $\boldsymbol{D}^H$, i.e. the Hermitian transpose of the original differential operator $\boldsymbol{D}$. This relation makes the derivation of the adjoint stability problem a straightforward task since no integrations by parts are necessary for chordwise differentiation operators.

### 5.2. *Adjoint equations*

The process of finding the adjoint stability equations simplifies to a matrix transposition for the chordwise operators and to repeated integration by parts in

$y$ for the wall-normal operators. Choosing the following boundary conditions for the adjoint problem:

$$\tilde{u}^+ = \tilde{v}^+ = \partial_y \tilde{v}^+ = 0 \quad \text{at} \quad y = 0 \quad \text{and} \quad \infty$$

eliminates the terms stemming from the integration by parts.

Omitting algebraic manipulations we can now state the adjoint global stability problem in the form

$$\begin{pmatrix} \boldsymbol{P}^+_{0,0} & & & & & & & & \\ \boldsymbol{P}^+_{0,2} & \boldsymbol{P}^+_{2,2} & & & & & & & \\ \boldsymbol{P}^+_{0,4} & \boldsymbol{P}^+_{2,4} & \ddots & & & & & & \\ & \boldsymbol{P}^+_{2,6} & \ddots & \ddots & & & & & \\ & & \ddots & \ddots & \ddots & & & & \\ & & & & \boldsymbol{P}^+_{1,1} & & & & \\ & & & & \boldsymbol{P}^+_{1,3} & \boldsymbol{P}^+_{3,3} & & & \\ & & & & \boldsymbol{P}^+_{1,5} & \boldsymbol{P}^+_{3,5} & \ddots & & \\ & & & & & \boldsymbol{P}^+_{3,7} & \ddots & \ddots & \\ & & & & & & \ddots & \ddots & \ddots \end{pmatrix} \begin{pmatrix} \boldsymbol{q}^+_0 \\ \boldsymbol{q}^+_2 \\ \vdots \\ \boldsymbol{q}^+_1 \\ \boldsymbol{q}^+_3 \\ \vdots \end{pmatrix}$$

$$= -\mathrm{i}\beta Re\mu \begin{pmatrix} \boldsymbol{Q}^+_{0,0} & & & & & & & & \\ \boldsymbol{Q}^+_{0,2} & \boldsymbol{Q}^+_{2,2} & & & & & & & \\ & \boldsymbol{Q}^+_{2,4} & \ddots & & & & & & \\ & & \ddots & \ddots & & & & & \\ & & & & \boldsymbol{Q}^+_{1,1} & & & & \\ & & & & \boldsymbol{Q}^+_{1,3} & \boldsymbol{Q}^+_{3,3} & & & \\ & & & & & \boldsymbol{Q}^+_{3,5} & \ddots & & \\ & & & & & & \ddots & \ddots & \end{pmatrix} \begin{pmatrix} \boldsymbol{q}^+_0 \\ \boldsymbol{q}^+_2 \\ \vdots \\ \boldsymbol{q}^+_1 \\ \boldsymbol{q}^+_3 \\ \vdots \end{pmatrix}, \qquad (5.9)$$

where

$$\boldsymbol{P}^+_{m,n} = \begin{cases} S^+_{0,n} & \text{for } m = 0,\ n = 0 \\ \begin{pmatrix} S^+_{0,n-1} \\ S^+_{0,n} \end{pmatrix} & \text{for } m = 0,\ n > 0 \\ \begin{pmatrix} R^+_{m-1,n-1} & S^+_{m,n-1} \\ R^+_{m-1,n} & S^+_{m,n} \end{pmatrix} & \text{for } m > 0,\ n > 0, \end{cases}$$

and

$$\boldsymbol{Q}^{+}_{m,n} = \begin{cases} a_{0,0}\beta^2 & \text{for } m = n = 0 \\ \begin{pmatrix} a_{0,1}\partial_y \\ 0 \end{pmatrix} & \text{for } m = 0,\ n = 2 \\ \begin{pmatrix} a_{m-1,0}\left(\beta^2 - \partial_y^2\right) & 0 \\ a_{m-1,1}\partial_y & a_{m,0}\beta^2 \end{pmatrix} & \text{for } m = n > 0 \\ \begin{pmatrix} 0 & a_{m,1}\partial_y \\ 0 & -a_{m,2} \end{pmatrix} & \text{for } m = (n-2) > 0. \end{cases}$$

The adjoint operators $R^{+}_{m,n}$ and $S^{+}_{m,n}$ are

$$\begin{aligned} R^{+}_{m-1,m-1} &= a_{m-1,0}\left[(\mathscr{L}^{+}_{y} + (m-2)V')\left(\partial_y^2 - \beta^2\right) + mV''\partial_y + 2V'\partial_y^2 + 2\mathrm{i}\beta ReW'\partial_y\right], \\ R^{+}_{m-1,m} &= a_{m-1,1}[-(\mathscr{L}^{+}_{y} + (m-1)V')\partial_y], \\ R^{+}_{m-1,m+1} &= a_{m-1,2}\left[(1+V')\left(\partial_y^2 - \beta^2\right) + V''\partial_y\right], \\ R^{+}_{m-1,m+2} &= a_{m-1,3}[-(1+V')\partial_y], \\ S^{+}_{m,m-1} &= a_{m-1,1}[-\beta^2 V''], \\ S^{+}_{m,m} &= a_{m,0}[-\beta^2(\mathscr{L}^{+}_{y} + (m+1)V')], \\ S^{+}_{m,m+1} &= a_{m,1}[-(\mathscr{L}^{+}_{y} + (m+2)V')\partial_y - 2\mathrm{i}\beta ReW' - (m+2+\beta^2)V''], \\ S^{+}_{m,m+2} &= a_{m,2}[(\mathscr{L}^{+}_{y} + (m+1)V') - \beta^2(1+V')], \\ S^{+}_{m,m+3} &= a_{m,3}[-(1+V')\partial_y - V''], \\ S^{+}_{m,m+4} &= a_{m,4}[1+V'], \end{aligned}$$

with

$$\mathscr{L}^{+}_{y} = \partial_y^2 + V\partial_y + V' - \beta^2 + \mathrm{i}\beta ReW$$

and

$$a_{m,n} = \sqrt{\frac{(m+n)!}{m!}}.$$

Again, we obtain a coupled system of local stability problems.

### 5.3. *Adjoint eigenfunctions of swept Hiemenz flow*

The upper triangular structure of the regular global stability problem (see Part 1) allowed us to first solve for the eigenvalues of the block diagonal terms. The eigenfunctions of the diagonal sub-problems produced right-hand sides for the lower-order Hermite coefficients, whereas the right-hand sides for the higher-order Hermite terms were identically zero. As a consequence, the eigenfunctions had a polynomial dependence on the chordwise direction.

In the adjoint problem (5.9) the operator matrix is lower triangular. We can still compute the eigenvalues (which will be the complex conjugates of the original problem) by solving the block diagonal sub-problems. The adjoint eigenfunctions, however, will not be polynomials, but rather will be represented by infinite Hermite series, whose first $N-1$ coefficients are identically zero, since lower-order solutions

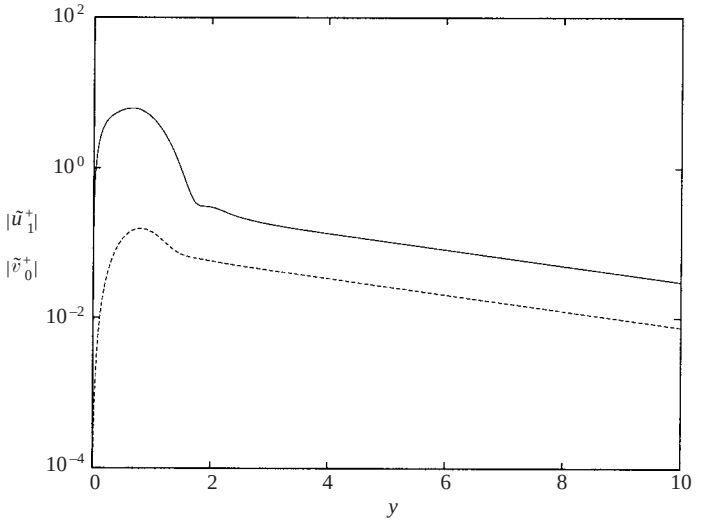


FIGURE 12. Absolute values of the first term of the eigenfunction that is adjoint to the most unstable mode for $Re = 800$ and $\beta = 0.25$: ——, $|u_1^+|$; – – –, $|v_0^+|$.

force higher-order subsystems:

$$\begin{pmatrix} \hat{u}^+ \\ \hat{v}^+ \end{pmatrix} = \sum_{n=N}^{\infty} \begin{pmatrix} \tilde{u}_n^+ \mathrm{He}_n(x) \\ \tilde{v}_{n-1}^+ \mathrm{He}_{n-1}(x) \end{pmatrix}. \tag{5.10}$$

In practice, we will truncate this infinite series at order $n > N$.

Figure 12 shows the lowest-order term of the adjoint eigenfunction corresponding to the most unstable mode for $Re = 800$ and $\beta = 0.25$. By construction, this adjoint eigenfunction is orthogonal to all regular eigenfunctions of order $N = 1$ except to the one associated with the most unstable mode. We note that $|\tilde{u}_1^+| \gg |\tilde{v}_0^+|$, contrary to what is observed for the most unstable regular mode (see Part 1). It is also remarkable that both $\tilde{u}_1^+$ and $\tilde{v}_0^+$ are exponentially decaying in the free stream, unlike the most unstable regular mode (or all discrete regular modes for that matter) which exhibits super-exponential decay for $u_1$. This effect is due to the transposition of the diagonal operator $\boldsymbol{P}_{1,1}$ ($\boldsymbol{P}_{1,1}^+$, respectively), which couples the equation for $u_1^+$ to the equation for $v_0^+$ in the free stream.

The first four terms of the infinite Hermite series are displayed together in figure 13. The most striking feature of this plot is that the terms of the Hermite series (5.10) become larger with increasing order $n$. In fact, it can be shown that the Hermite series (5.10) is divergent, which follows immediately from estimating the terms of the Hermite series as

$$\tilde{u}_n^+, \tilde{v}_{n-1}^+ \sim \sqrt{n!}.$$

This divergence does not allow a closed-form representation of the adjoint eigenfunction $(\hat{u}^+(x, y), \hat{v}^+(x, y))^T$. Nevertheless, we will demonstrate that the divergent series (5.10) can still provide meaningful results.

### 5.4. *Borel summation of the divergent Hermite series*

We learned previously that we can use the eigenfunctions of the adjoint problem, $\boldsymbol{q}^+(x, y)$, to extract the amplitude $A$ of the associated regular mode $\boldsymbol{q}(x, y)$ from an arbitrary velocity field $\boldsymbol{f}(x, y) = (\hat{u}(x, y), \hat{v}(x, y))^T$. We project the velocity field

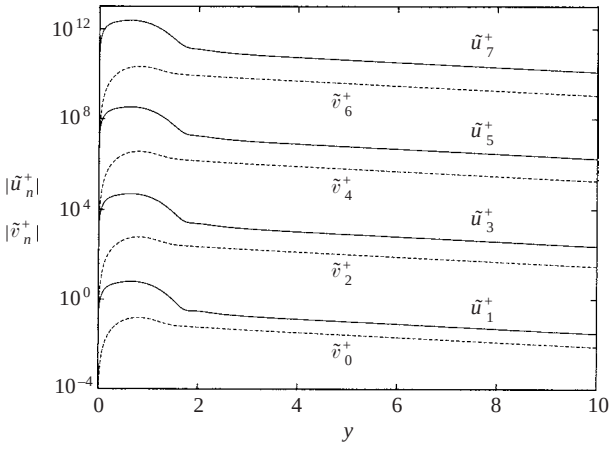


FIGURE 13. Absolute values of the first four terms of the eigenfunction that is adjoint to the most unstable mode for $Re = 800$ and $\beta = 0.25$: ——, $|u_n^+|$; – – –, $|v_n^+|$.

$\boldsymbol{f}(x, y)$ onto the adjoint eigenfunction $\boldsymbol{q}^+$ with

$$A = \left(\boldsymbol{q}^+, \boldsymbol{L}\boldsymbol{f}\right)_{\tilde{H}},$$

where $\boldsymbol{L}$ is the matrix operator on the right-hand side of the linear stability problem (see Part 1). We find that we can express $\boldsymbol{L}\boldsymbol{f}$ using the streamwise and wall-normal vorticities, $\boldsymbol{L}\boldsymbol{f} = \beta^2 Re(\hat{\psi}, -\hat{\omega})^T$. Thus we obtain

$$A = \int_{-\infty}^{\infty}\int_{0}^{\infty} \beta^2 Re[(\hat{v}^+(x, y))^* \hat{\psi}(x, y) - (\hat{u}^+(x, y))^* \hat{\omega}(x, y)]\, \mathrm{d}x\, \mathrm{d}y$$

and, using the Hermite series representations, this results in

$$A = \int_{0}^{\infty} \beta^2 Re \sum_{n=N}^{\infty} \underbrace{[(\tilde{v}_{n-1}^+(y))^* \tilde{\psi}_{n-1}(y) - (\tilde{u}_n^+(y))^* \tilde{\omega}_n(y)]}_{\tilde{a}_n(y)}\, \mathrm{d}y. \tag{5.11}$$

We recall from the previous section that the Hermite coefficients of the adjoint eigenfunctions grow like $\sqrt{n!}$. Spectral convergence guarantees that the coefficients $\tilde{\psi}_{n-1}$ and $\tilde{\omega}_n$ decay exponentially like $\exp(-\alpha n)$ with $\alpha$ positive and $O(1)$ (see, e.g. Boyd 1984). Thus, the coefficients $\tilde{a}_n(y)$ behave like

$$\tilde{a}_n(y) \sim \sqrt{n!}\mathrm{e}^{-\alpha n} \quad \text{as} \quad n \to \infty.$$

Consequently, the series (5.11) diverges. To find an asymptotic result for the sum we use Borel summation (see Bender & Orszag 1978) where we define a new series $\phi(\xi)$,

$$\phi(\xi) = \sum_{n=0}^{\infty} \frac{\tilde{a}_n \xi^n}{n!},$$

with $\tilde{a}_n = 0$ for $n < N$. As $n \to \infty$ the terms of this series behave like

$$\frac{\tilde{a}_n \xi^n}{n!} \sim \frac{\xi^n \mathrm{e}^{-\alpha n}}{\sqrt{n!}},$$

and, as a result, the series converges for sufficiently small $\xi$. We then define the Borel integral

$$B(\xi) = \int_{0}^{\infty} \mathrm{e}^{-\tau} \phi(\xi\tau)\, \mathrm{d}\tau. \tag{5.12}$$

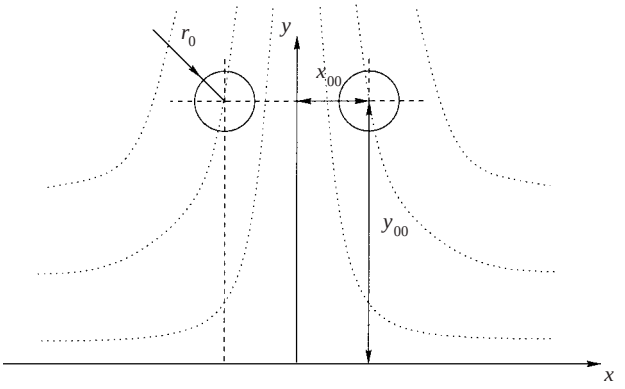


FIGURE 14. Initial condition for the DNS of an incoming vortex pair.

For $\xi \to 0$ this integral can be expanded as

$$B(\xi) \sim \sum_{n=0}^{\infty} \tilde{a}_n \xi^n.$$

This power series is asymptotic to $B(\xi)$ as $\xi \to 0$, and it is identical to our divergent series for $\xi = 1$. We thus choose to approximate our divergent sum by $B(1)$. In practice, the above technique involves the following steps: ($a$) evaluate the convergent sum $\phi(\xi)$ for various $\xi > 0$, ($b$) find the asymptotic behaviour of $\phi(\xi \to 0)$, and ($c$) evaluate $B(1)$, where we substitute the asymptotic behaviour for $\phi(t)$ into (5.12).

This algorithm enables us to find asymptotic results for the divergent sum in (5.11). To obtain the amplitude $A$ it remains to evaluate the integral with respect to $y$. The next section will demonstrate and apply the algorithm outlined above to a numerical receptivity experiment.

## 6. A receptivity experiment

Along with the theoretical results of the previous sections we wish to present numerical experiments to investigate the receptivity of swept attachment-line boundary layer flow to vortical disturbances in the free stream. Following an approach taken by Bertolotti (1997), we decompose the flow field into a base flow $\boldsymbol{U}$ (swept Hiemenz flow), a free-stream disturbance $\boldsymbol{u}_V$, and boundary layer disturbances $\boldsymbol{u}_B$,

$$\boldsymbol{u}(x, y, z, t) = \boldsymbol{U}(x, y) + \boldsymbol{u}_V(x, y, z, t) + \boldsymbol{u}_B(x, y, z, t).$$

For the free-stream disturbance $\boldsymbol{u}_V$ we choose a pair of spanwise vortices. The vortex pair is initially located far away from the wall. The pair is centred with respect to $x = 0$ yielding (anti-)symmetric initial conditions (see figure 14). Each of the two vortices initially corresponds to an Oseen vortex (Albring 1981) with a spanwise vorticity distribution $\theta$ according to

$$\theta = A \frac{2}{r_0^2} \mathrm{e}^{-r^2/r_0^2}. \tag{6.1a}$$

This vorticity distribution induces an azimuthal velocity $v_a$,

$$v_a = \frac{A}{r}\left(1 - \mathrm{e}^{-r^2/r_0^2}\right), \tag{6.1b}$$

where $r$ is the distance from the vortex centre $(x_0, y_0)$,

$$r = \sqrt{(x - x_0)^2 + (y - y_0)^2}.$$

The parameter $r_0$ determines the width of the vortex core. The Oseen vortex is independent of the spanwise coordinate $z$ and would therefore induce only disturbances with spanwise wavenumber $\beta = 0$, which are known to be stable. To introduce a disturbance with non-zero spanwise wavenumber we add an eccentricity to the vortex centre by letting

$$x_0 = x_{00} + r_{00}\cos\beta z,$$
$$y_0 = y_{00} + r_{00}\sin\beta z.$$

This generates a helical spanwise vortex. It is important to realize that such a helical vortex does not consist of a single spanwise Fourier mode $\beta$. Rather, it represents a wavepacket with its power spectrum centred about $\beta$.

An Oseen vortex does not satisfy the no-slip conditions at the wall. To remedy this we take the following three steps:

(*a*) We choose $y_{00} \gg 1$ such that at the wall $v_a = O(y_{00}^{-1})$ is small.

(*b*) For each vortex with amplitude $A$ centred at $(x_{00}, y_{00})$ we superimpose a virtual vortex with $-A$ and $(x_{00}, -y_{00})$. This ensures that $v = \partial_y v = 0$ at the wall. However, this also has the unwanted effect of doubling the chordwise velocity component $u$ at $y = 0$.

(*c*) To satisfy $u|_{y=0} = 0$ we multiply the chordwise component of the initial flow field by the base flow component $U(y)$. This leaves the flow unchanged outside the boundary layer but forces $u$ smoothly to zero within the boundary layer.

These three modifications result in initial conditions that can be used to introduce localized vortices into our direct numerical simulations. We observe a short transient effect at the beginning of the simulations during which the flow adjusts; the significant features of the initial condition, however, persist.

By choosing different signs for the rotation of the two vortices we can construct three different configurations. By giving both vortices (i) the same sense of rotation we create a configuration that can be decomposed into even modal solutions ($u$ symmetric, $v$ and $w$ antisymmetric). Two counter-rotating vortices yield odd initial conditions. In this configuration the vortex pair either induces a velocity that (ii) accelerates the impingement of the vortices on the wall, or the impingement is (iii) decelerated by the self-induced velocity field.

We present simulations of all three cases. For these experiments we choose the following set of parameters:

$$Re = 800, \quad \beta = 0.25, \quad A = 10^{-6}, \quad x_{00} = 20, \quad y_{00} = 100, \quad r_0 = 10, \quad r_{00} = 1.$$

With our choice of $Re$ and $\beta$ we make sure that the flow is linearly unstable. The remaining simulation parameters are

$$N_x = 320, \quad N_y = 193, \quad N_z = 16, \quad L_x = 400, \quad L_z = 8\pi, \quad y_{\max} = 1000, \quad y_{\text{half}} = 10.$$

Figure 15 shows the evolution of the vorticity field throughout the entire simulation for decelerated odd initial conditions (case (iii)).

The vortices are advected along the streamlines of the stagnation point flow (indicated by dotted lines). As the two vortices reach the chordwise extent of the computational domain a fringe region dissipates the disturbances. The chordwise stretching of the vortices is related to the strain rate $S^*$ of the stagnation-point flow. For the two other configurations of initial conditions, cases (i) and (ii), the evolution of the outer flow field is nearly indistinguishable from the evolution shown in figure 15. Nonlinear effects on the vortex evolution are weak in all three simulations owing to the small amplitude $A$.

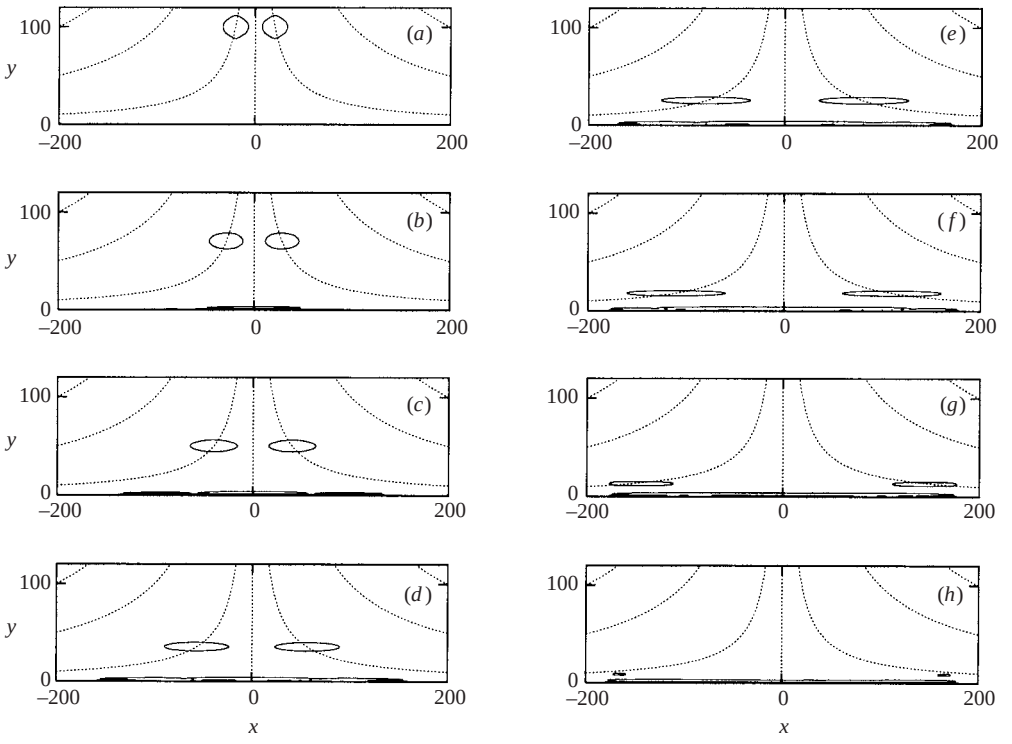


FIGURE 15. Evolution of the vorticity field during the DNS; the solid curves are the locations where the vorticity vector has length $10^{-8}$: (*a*) $t = 0$, (*b*) $t = 279$, (*c*) $t = 557$, (*d*) $t = 836$, (*e*) $t = 1114$, (*f*) $t = 1393$, (*g*) $t = 1671$, (*h*) $t = 2000$.

The interaction of the two vortices with the wall creates disturbances in the boundary layer. Their vorticity levels are significantly higher than the vorticity in the two vortex cores. The generated boundary layer vorticity is hardly visible in figure 15 due to the scale of the plots, but we observe that the disturbances in the boundary layer persist even after the vortex pair has left the computational domain.

We will attempt to quantify these disturbances by defining two energy measures for the spanwise Fourier mode $\beta$: a total energy $\hat{e}_{\mathrm{tot}}$ as was already suggested in § 2,

$$\hat{e}_{\mathrm{tot}} = \int_{-L/2}^{L/2} \mathrm{d}x \int_0^{\infty} \tfrac{1}{2}(\hat{u}_\beta^* \hat{u}_\beta + \hat{v}_\beta^* \hat{v}_\beta + \hat{w}_\beta^* \hat{w}_\beta)\,\mathrm{d}y,$$

and a boundary layer energy $\hat{e}_{\mathrm{BL}}$,

$$\hat{e}_{\mathrm{BL}} = \int_{-L/2}^{L/2} \mathrm{d}x \int_0^{\delta_{\mathrm{BL}}} \tfrac{1}{2}(\hat{u}_\beta^* \hat{u}_\beta + \hat{v}_\beta^* \hat{v}_\beta + \hat{w}_\beta^* \hat{w}_\beta)\,\mathrm{d}y.$$

We choose $L = 200$ — large enough to include all important features of the flow, yet sufficiently small to exclude any effects from the fringe region. The upper bound $\delta_{\mathrm{BL}}$ is set to 1 so that $\hat{e}_{\mathrm{BL}}$ measures only the disturbances within the interval $y \in [0, 1]$.

Figure 16 shows the temporal evolution of these two energy measures for the three different configurations. The energy curves for the two odd configurations are indistinguishable. The total energy $e_{\mathrm{tot}}$ reaches a maximum at about $t = 1100$. This maximum coincides with the time of impingement at which the vortices begin to move predominantly in the chordwise direction. The total energy then decays monotonically

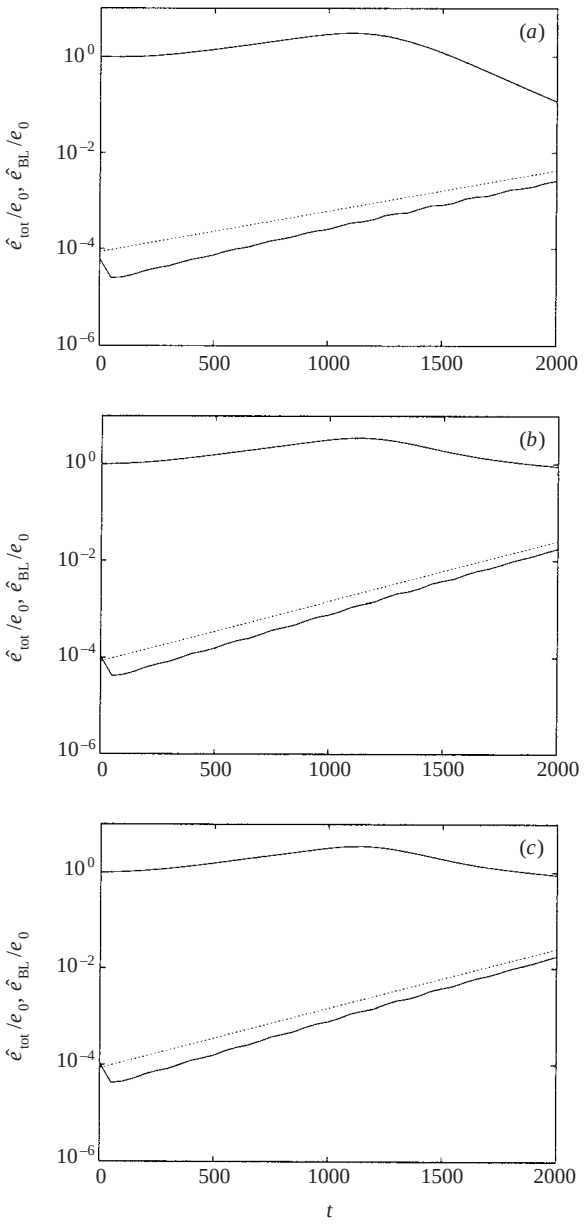


FIGURE 16. Energies $\hat{e}_{\rm tot}$ and $\hat{e}_{\rm BL}$ normalized by $e_0 = \hat{e}_{\rm tot}|_{t=0}$ plotted against time for (*a*) even, (*b*) odd accelerated, (*c*) odd decelerated initial conditions; the thin dotted line shows the theoretical growth of the most unstable mode (*a*) even, (*b*,*c*) odd mode.

as the vortices leave the computational domain. The odd configurations exhibit less decay than the even counterpart. At $t = 2000$ (the vortices have left the computational domain) the total energy of the odd configurations is nearly at the initial energy level $e_0$, whereas in the even configuration 90% of the disturbance energy has been advected out of the computational domain.

After a transient period (up to $t \approx 50$) the boundary layer energy $e_{\rm BL}$ grows exponentially for all three cases. The growth rate is comparable to the growth rate of the respective most unstable modal solution. We also notice that $e_{\rm BL}$ grows faster for the

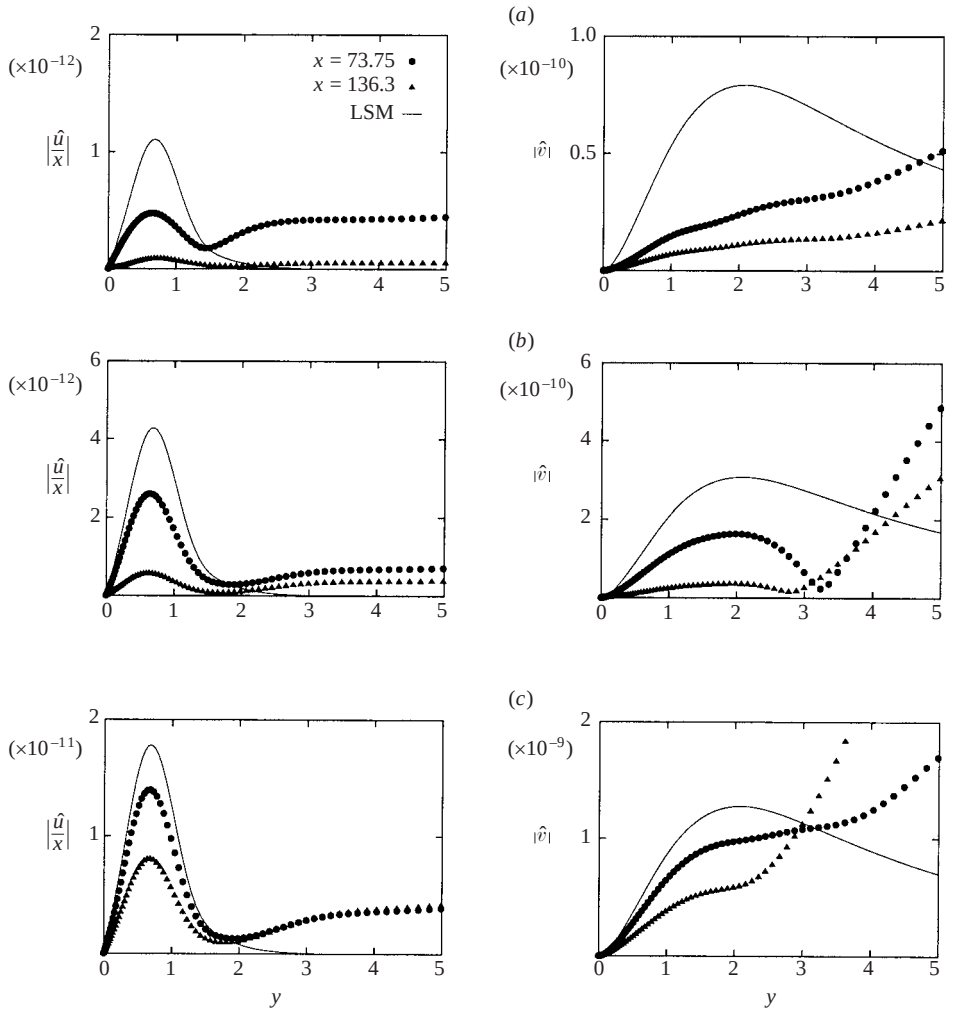


FIGURE 17. Cuts at $x = 73.75$ and $x = 136.3$ of the spanwise mode $\beta$ of the velocity field of case (*c*) for (*a*) $t = 50$, (*b*) $t = 1000$, (*c*) $t = 2000$.

odd cases than for the even case. At the end of the simulation more energy from the vortices has been absorbed by the boundary layer disturbances in the odd cases.

These results suggest that we feed energy from an outer vortical disturbance into the boundary layer, and that this process appears more efficient for odd initial conditions. The growth rates of $e_{\mathrm{BL}}$ further suggest that the respective most unstable modes were excited.

To further investigate the flow field for case (iii), we take cuts at two different chordwise locations of the spanwise Fourier mode $\beta$ of the velocity field and plot the result versus the wall-normal coordinate $y$ (figure 17). The chordwise velocity component $\hat{u}$ is divided by $x$ to eliminate the linear chordwise dependence. The shape of the most unstable mode is added (as a solid line) for comparison. At $t = 50$ the flow differs significantly from the most unstable mode; at $t = 2000$, however, the flow within the boundary layer ($y < 3$) resembles the most unstable mode markedly better. In particular, the chordwise structure resembles the most unstable mode, i.e.

$\hat{u}$ depends almost linearly on $x$ and $\hat{v}$ is nearly constant in $x$. Outside the boundary layer we notice strong disturbances caused by the recent passing of the vortices.

This numerical experiment presents an opportunity to validate the adjoint operator method that was introduced in the previous section. To this end we take the flow field at $t=0$ for the three different cases and use the adjoint solutions to extract the amplitude of the most unstable mode (either even or odd). Following the steps outlined for the Borel summation of the resulting divergent series we find the following asymptotic behaviour for the modified series $\phi(\xi)$ as $\xi \to 0$:

$$\phi(\xi) \sim \begin{cases} A_o & \text{for the odd cases} \\ A_e \xi & \text{for the even case.} \end{cases}$$

Substituting this result into (5.12) and evaluating the integral for $\xi = 1$ gives an asymptotic approximation for the sum of the divergent series. The amplitudes $A$ for the three cases follow immediately from that. We then calculate the boundary layer energy $e_{\mathrm{BL}}$ that would result from taking into account only the single most unstable mode with the initial amplitude just computed. The thin dotted lines in figure 16 show these computed boundary layer energies $e_{\mathrm{BL}}$. The theoretically computed amplitudes predict the boundary layer energy very well throughout the temporal extent of the simulations. For large times the boundary layer energy of the direct numerical simulations closely approaches the theoretical curve, which supports the observation that the vortex pair has excited the most unstable mode. The computed amplitudes were also used to scale the solid lines in figure 17.

## 7. Summary and conclusions

A non-modal stability analysis of swept attachment-line boundary layer flow has been presented based on the transient amplification of kinetic perturbation energy. Although no transient energy growth has been found for discrete uniform modes, significant amplification has been observed for disturbances consisting of discrete Görtler–Hämmerlin-modes or higher-order modes. In fact, as the order $N$ of the discrete modes increases, unbounded energy growth is theoretically possible which is only limited by the amplitude criterion for higher-order modes based on the validity of the assumptions underlying the linearization step (see Part 1). The role of algebraically decaying modes has been investigated and found to be of a catalytic nature, i.e. transient growth of algebraically decaying modes is rather benign; however, when combined with discrete modes, significantly higher energy amplification can be achieved compared to disturbances consisting merely of discrete modes. All findings have been confirmed by careful direct numerical simulations.

A mathematical framework for analysing receptivity has been derived based on the adjoint formulation of the global stability problem. Again, an expansion in Hermite polynomials yields separability in the chordwise direction which in turn results in coupled local stability problems. In contrast to the direct stability problem, the solutions to the adjoint stability equations are no longer polynomials in the chordwise direction and, in addition, exhibit weaker exponential decay in the free stream. When using the adjoint eigenfunctions in a receptivity analysis one encounters divergent series for the receptivity coefficient. Nevertheless, this problem can be overcome by applying Borel summation, and physically meaningful receptivity measures can easily be computed. A numerical receptivity experiment aimed at demonstrating the use of adjoint solutions investigated the excitation of boundary layer disturbances by free-stream vortices convected by the mean flow. A marked response in the least stable

boundary layer mode was found, and the amplitude of excitation closely agreed with theoretical predictions. It is worth mentioning that the adjoint formulation of the global stability problem presented in this paper could also be used as a fundamental building block in the study of feedback control mechanisms for manipulating, delaying or suppressing disturbance growth in swept attachment-line boundary layer flow. A study of this type is left for a future effort.

We would like to thank Cray Inc. for financial support through an industrial student fellowship. D.O. would like to thank Professor R. Friedrich from TU München and Professors V. Theofilis and U. Dallmann from DLR Göttingen. A significant part of this work was accomplished during visits at the TU München and DLR Göttingen.

## REFERENCES

Albring, W. 1981 *Elementarvorgänge fluider Wirbelbewegungen.* Akademie-Verlag, Berlin.

Bender, C. M. & Orszag, S. A. 1978 *Advanced Mathematical Methods for Scientists and Engineers.* McGraw-Hill.

Bergström, L. 1993 Optimal growth of small disturbances in pipe Poiseuille flow. *Phys. Fluids* A **5**, 2710–2720.

Bertolotti, F. P. 1997 Response of the Blasius boundary layer to free-stream vorticity. *Phys. Fluids* **9**, 2286–2299.

Boberg, L. & Borsa, U. 1988 Onset of turbulence in a pipe. *Z. Naturforsch.* **43a**, 697–726.

Boyd, J. P. 1984 Asymptotic coefficients of Hermite functions series. *J. Comput. Phys.* **54**, 382–410.

Butler, K. M. & Farrell, B. F. 1992 Three-dimensional optimal perturbations in viscous shear flow. *Phys. Fluids* A **4**, 1637–1650.

Choudhari, M. 1996 Boundary-layer receptivity to three-dimensional unsteady vortical disturbances in the free stream. *AIAA Paper* 96-0181.

Corbett, P. & Bottaro, A. 2000 Optimal perturbations for boundary layers subject to streamwise pressure gradient. *Phys. Fluids* **12**, 120–130.

Crouch, J. D. 1992*a* Localized receptivity of boundary layers. *Phys. Fluids* A **4**, 1408–1414.

Crouch, J. D. 1992*b* Non-localized receptivity of boundary layers. *J. Fluid Mech.* **244**, 567–581.

Farrell, B. F. 1989 Optimal excitation of baroclinic waves. *J. Atmos. Sci.* **46**, 3279–3288.

Farrell, B. F. & Ioannou, P. J. 1993 Transient development of perturbations in stratified shear flow. *J. Atmos. Sci.* **50**, 2201–2214.

Foster, R. C. 1997 Structure and energetics of optimal Ekman layer perturbations. *J. Fluid Mech.* **333**, 97–123.

Goldstein, M. E. & Hultgren, L. S. 1989 Boundary-layer receptivity to long-wave freestream disturbances. *Annu. Rev. Fluid Mech.* **21**, 137–166.

Gustavsson, L. H. 1991 Energy growth of three-dimensional disturbances in plane Poiseuille flow. *J. Fluid Mech.* **224**, 241–260.

Hill, D. C. 1995 Adjoint systems and their role in the receptivity problem for boundary layers. *J. Fluid Mech.* **292**, 183–204.

Hristova, H., Roch, S., Schmid, P. J. & Tuckerman, L. 2002 Transient growth in Taylor-Couette flow. *Phys. Fluids* **14**, 3475–3484.

Huerre, P. & Monkewitz, P. A. 1990 Local and global instabilities in spatially developing flows. *Annu. Rev. Fluid Mech.* **22**, 473–537.

Jacobs, R. G. & Henningson, D. S. 1999 Evaluation of data from direct numerical simulations of transition due to freestream turbulence. *Ann. Research Briefs, CTR-Stanford.*

Kelvin, Lord 1887 Stability of fluid motion – Rectilinear motion of viscous fluid between two parallel flows. *Phil. Mag.* **24**, 188–196.

Luchini, P. & Bottaro, A. 1998 Görtler vortices: a backward-in-time approach to the receptivity problem. *J. Fluid Mech.* **363**, 1–23.

Meseguer, A. 2002 Nonnormal effects in the Taylor–Couette problem. *Theor. Comput. Fluid Dyn.* **16**, 71–77.

Obrist, D. 2000 On the stability of the swept leading-edge boundary layer. PhD dissertation, University of Washington.

Obrist, D. & Schmid, P. J. 2003 On the linear stability of swept attachment-line boundary layer flow. Part 1. Spectrum and asymptotic behaviour. *J. Fluid Mech.* **493**, 1–29.

Orr, W. M. F. 1907 The stability or instability of the steady motions of a perfect liquid and of a viscous liquid. Part I: A perfect liquid. Part II: A viscous liquid. *Proc. R. Irish Acad.* A **27**, 9–138.

Reddy, S. C. & Henningson, D. S. 1993 Energy growth in viscous channel flows. *J. Fluid Mech.* **252**, 209–238.

Schmid, P. J. & Henningson, D. S. 1994 Optimal energy density growth in Hagen–Poiseuille flow. *J. Fluid Mech.* **277**, 197–225.

Schmid, P. J. & Henningson, D. S. 2001 *Stability and Transition in Shear Flows.* Springer.

Schmid, P. J., Henningson, D. S., Khorrami, M. & Malik, M. 1993 A sensitivity study of hydrodynamic stability operators. *Theor. Comput. Fluid Dyn.* **4**, 227–240.

Schmid, P. J. & Kytömaa, H. K. 1994 Transient and asymptotic stability of granular flow. *J. Fluid Mech.* **264**, 255–275.

Trefethen, A. E., Trefethen, L. N. & Schmid, P. J. 1999 Spectra and pseudospectra for pipe Poiseuille flow. *Comput. Meth. Appl. Mech. Engng* **175**, 413–420.

Trefethen, L. N., Trefethen, A. E., Reddy, S. C. & Driscoll, T. A. 1993 Hydrodynamic stability without eigenvalues. *Science* **261**, 578–584.

Türkyilmazoğlu, M. & Gajjar, J. S. B. 1999 On the absolute instability of the attachment-line and swept Hiemenz boundary layers. *Theor. Comput. Fluid Dyn.* **13**, 57–75.

Waleffe, F. 1995 Transition in shear flows: non-linear normality versus non-normal linearity. *Phys. Fluids* **7**, 3060–3066.